

Abundant (110) Facets on PdCu₃ Alloy Promote Electrochemical Conversion of CO₂ to CO

Jianwu Dong,[○] Ying Cheng,[○] Ying Li,[○] Xianyun Peng, Rui Zhang, Hsiao-Tsu Wang, Chunyang Wang, Xiaoyan Li, Pengfei Ou, Chih-Wen Pao, Lili Han,* Way-Faung Pong, Zhang Lin, Jun Luo, and Huolin L. Xin*



Cite This: *ACS Appl. Mater. Interfaces* 2022, 14, 41969–41977



Read Online

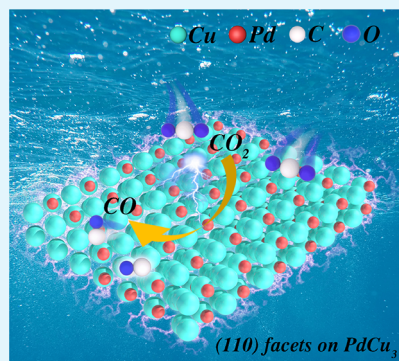
ACCESS |

Metrics & More

Article Recommendations

Supporting Information

ABSTRACT: Electrochemical conversion of CO₂ to high-value chemical fuels offers a promising strategy for managing the global carbon balance but faces huge challenges due to the lack of effective electrocatalysts. Here, we reported PdCu₃ alloy nanoparticles with abundant exposed (110) facets supported on N-doped three-dimensional interconnected carbon frameworks (PdCu₃/NC) as an efficient and durable electrocatalyst for electrochemical CO₂ reduction to CO. The catalyst exhibits extremely high intrinsic CO₂ reduction selectivity for CO production with a Faraday efficiency of nearly 100% at a mild potential of −0.5 V. Moreover, a rechargeable high-performance Zn–CO₂ battery with PdCu₃/NC as a cathode is developed to deliver a record-high energy efficiency of 99.2% at 0.5 mA cm^{−2} and rechargeable stability of up to 133 h. Theoretical calculations elucidate that the exposed (110) facet over PdCu₃/NC is the active center for CO₂ activation and rapid formation of the key *COOH intermediate.



KEYWORDS: CO₂ reduction reaction, exposed facet, CO product, alloy electrocatalyst, Zn–CO₂ battery

INTRODUCTION

The electrochemical carbon dioxide (CO₂) reduction into value-added chemicals under ambient conditions provides a feasible strategy to retard the depletion of fossil fuels and alleviate the greenhouse gas emission to mitigate the environment and energy crisis.^{1–3} Various CO₂ reduction reaction (CO₂RR) products can be achieved by different CO₂RR pathways, such as C₁ (CO, CH₄, HCOOH, etc.), C₂ (C₂H₄, C₂H₅OH, etc.), and even C₃ (C₃H₈O, etc.).^{4–8} Among them, the conversion of CO₂ to CO is one of the promising reaction pathways because it possesses great prospects in Zn–CO₂ battery, and the product, CO, can be easily separated from the aqueous electrolytes for further use.⁹ More importantly, CO as a fundamental chemical feedstock holds large market compatibility and a wide range of applications in chemicals, metallurgy, medicine, and so forth.^{10,11} Although many breakthroughs have been made in exploring various catalysts for the selective electrochemical conversion of CO₂ to CO, there are still huge challenges in terms of activity, selectivity, and long-term stability.

To realize the production of CO with high selectivity from CO₂RR, the proper binding strength of the *COOH intermediate is considered a pivotal point, which requires catalysts to bind *COOH strongly enough to facilitate the activation of CO₂ and *CO weakly enough to allow CO desorption readily from the catalyst surface.^{12,13} As widely studied electrocatalysts for CO₂RR, Cu-based nanomaterials

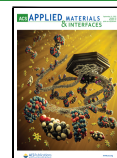
provide appropriate binding energy for reduction intermediates (*COOH) to minimize the energy barrier to this step.¹⁴ However, within the same potential range, they can also furnish suitable binding energies for other reduction intermediates, resulting in a wide variety of reduced products and low purity CO, making it difficult to use the CO product directly.¹⁵ Therefore, it is desirable to modify Cu-based catalysts for catalysis of CO₂RR to CO with high selectivity.

Alloying is one of the most promising approaches to adjusting the intrinsic performance of catalysts, which can change the surface strain and electronic structure of the alloy by controlling the atomic ratio. Therefore, alloying Cu with other metals for CO production with high selectivity could be a promising strategy. The metals, such as Au,^{16,17} Ag,^{18–20} Pd,^{21,22} and Zn,^{23,24} with high selectivity of CO₂RR to CO, have been selected for modifying Cu-based catalysts. Among them, Pd plays a key role in the improvement of CO generation on Cu-based catalysts because Pd can form a saturated Pd–H phase at near-zero potential, where CO₂ is more easily adsorbed on Pd–H,^{25,26} and control the d-band

Received: May 30, 2022

Accepted: August 28, 2022

Published: September 7, 2022



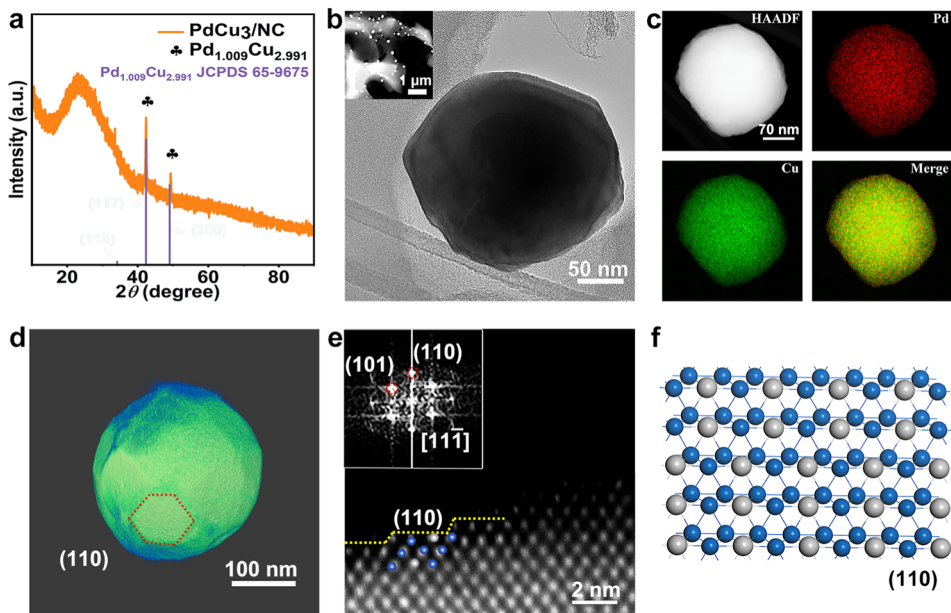


Figure 1. Morphology and structure characterizations of PdCu_3/NC . (a) XRD pattern. (b) TEM image, the inset is the low-magnification HAADF-STEM image. (c) HAADF-STEM and the corresponding EDS maps of Pd and Cu. (d) 3D reconstruction rendering of one PdCu_3 particle, which was achieved from 145 HAADF-STEM images at different tilt angles. (e) Atomic-resolution HAADF-STEM image and the corresponding FFT pattern (blue: Cu atoms; grey: Pd atoms). (f) Atomic structure model of the $\text{PdCu}_3(110)$ plane.

center of the active site and generate the key reduction intermediate, $^*\text{COOH}$, thereby realizing the selective production of CO from CO_2RR .^{27–29} However, the PdCu alloy catalyst still has competitive reactions in CO_2RR , such as the competition between the product formic acid and CO after the formation of the $^*\text{COOH}$ intermediate, the hydrogen evolution reaction and CO evolution in the same potential range, and so on.^{30,31} Therefore, it is necessary to improve the structure of PdCu alloys to reduce the effect of competing reactions on the production of CO from CO_2 .

Here, we designed and synthesized PdCu_3 alloy nanoparticles with abundant exposed (110) planes supported on N-doped three-dimensional interconnected carbon frameworks (PdCu_3/NC) according to our previously reported dissolution and carbonization method^{32,33} for highly efficient CO production from CO_2RR . The PdCu_3/NC catalyst achieved high selectivity for CO evolution with a Faradic efficiency (FE) of up to 99.8% at the applied potential of -0.5 V versus the reversible hydrogen electrode (vs RHE, all potentials in this work are given vs RHE unless stated otherwise.) in 0.1 M KHCO_3 electrolyte. Moreover, the PdCu_3/NC electrode was demonstrated to be an efficient cathode catalyst for a high-performance Zn– CO_2 battery with a maximum power density of 0.77 mW cm^{-2} , an open-circuit potential of 1.0 V, and energy efficiency of 99.2% at 0.5 mA cm^{-2} . In addition, up to 133 h of the long-term multicurrent step test proved its excellent rechargeable stability.

RESULTS AND DISCUSSION

Synthesis and Characterization. X-ray diffraction (XRD) pattern of the as-prepared PdCu_3/NC (Figure 1a) exhibits a typical tetragonal structure, where the two characteristic diffraction peaks at $2\theta = 42.3$ and 49.1° correspond to the (117) and (200) planes of PdCu_3 (JCPDS no. 65-9675),^{34,35} respectively. No other diffraction peaks of Pd and Cu can be observed, indicating the synthesis of high-

purity PdCu_3 alloy. Furthermore, the morphology and structure of the PdCu_3/NC were characterized by transmission electron microscopy (TEM). The high-angle annular dark-field scanning TEM (HAADF-STEM), TEM images, and size distribution diagram in Figures 1b, S1, and S2 show that nanoparticles with an average size of 220 ± 1.96 nm are distributed on the three-dimensional interconnected frameworks. The framework structure can greatly increase the N_2 adsorption volume, as demonstrated by the high specific surface area of $1416.05 \text{ m}^2 \text{ g}^{-1}$ and a pore volume of $0.711 \text{ cm}^3 \text{ g}^{-1}$ (Figure S3), which is beneficial to the mass transport of electrolytes in the process of CO_2RR .

The energy-dispersive X-ray spectroscopy (EDS) element mapping images in Figure 1c confirm that Pd and Cu atoms homogeneously distribute on the particles, and the Pd and Cu EDS maps are completely overlapped with the HAADF-STEM image, which evidences the formation of the PdCu_3 alloy. One PdCu_3 alloy particle was reconstructed and visualized in three dimensions (3D) by HAADF-STEM electron tomography (Figure 1d), which shows the faceted (110) surface exposed. The atomic-resolution HAADF-STEM images and the corresponding fast Fourier transform (FFT) pattern in Figure 1e show that the outermost crystal plane of PdCu_3 along the $[11\bar{1}]$ zone axis direction is the (110) crystal plane and has some stepped surfaces. The abundant (110) plane with a lattice spacing of 0.262 nm is further demonstrated by the high-resolution TEM image in Figure S1c, and its atomic structure model is shown in Figure 1f.

To study the electronic effects of Pd on Cu in the PdCu_3/NC , we conducted the X-ray photoelectron spectroscopy (XPS) analysis on PdCu_3/NC and control samples (Pd/NC and Cu/NC). Pd/NC and Cu/NC were prepared under the conditions similar to PdCu_3/NC , with the same moles of Pd for Pd/NC and Cu for Cu/NC as that of the total Pd and Cu for PdCu_3/NC (see the Experimental Section for more details). Their characterizations are shown in Figures S4 and

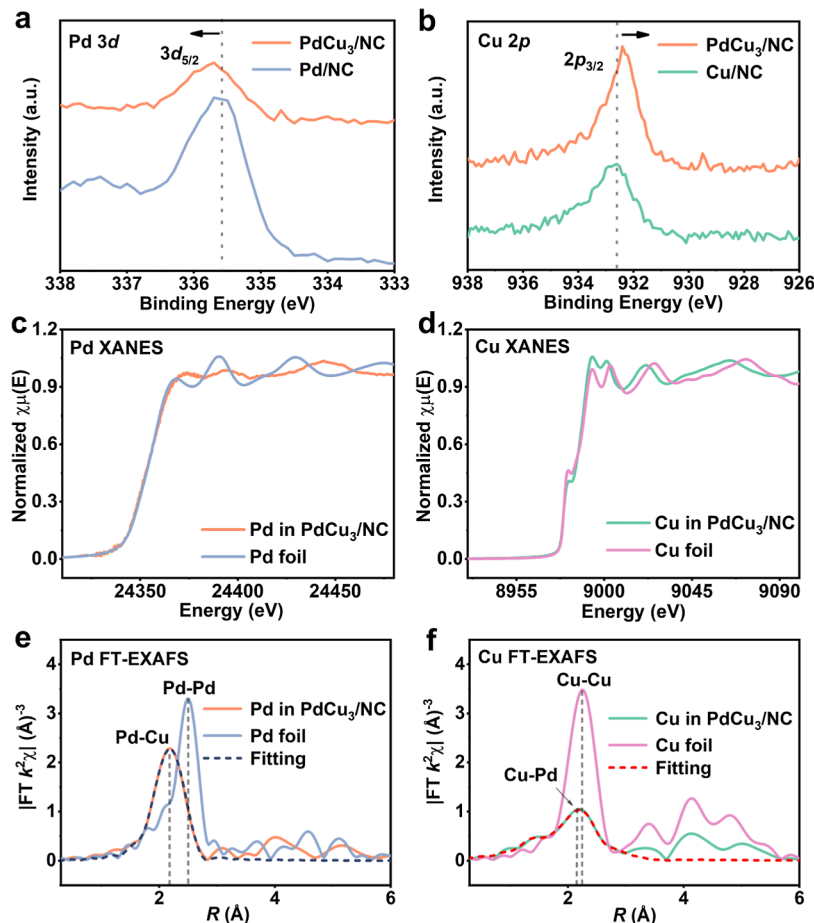


Figure 2. Synchrotron radiation X-ray absorption fine structure (XAFS) and XPS measurements for PdCu₃/NC. (a) High-resolution Pd 3d and (b) Cu 2p XPS spectra. (c) Pd K-edge XANES spectra of PdCu₃/NC and Pd foil. (d) Cu K-edge XANES spectra of PdCu₃/NC and Cu foil. The k^2 -weighted (e) Pd and (f) Cu K-edge FT-EXAFS spectra of PdCu₃/NC and their reference samples.

SS. The XPS spectra of PdCu₃/NC in Figure S6a show that the Pd 3d spectrum is divided into the Pd 3d_{5/2} and Pd 3d_{3/2} peaks, each of which is further split into two double peaks assigned to the Pd⁰ and Pd²⁺ chemical states, respectively.^{36,37} The peaks of Pd²⁺ could be attributed to the small amount of Pd dispersed on the carbon matrix in the form of ions. The ones of Pd⁰ could be contributed to by the metallic Pd in the PdCu₃ alloy. For the Cu 2p XPS spectrum, the two peaks at the binding energies of 932.4 and 951.3 eV (Figure S6b) could be assigned to Cu 2p_{3/2} and Cu 2p_{1/2}, respectively.^{38–40} Impressively, by comparing PdCu₃/NC with Pd/NC and Cu/NC (Figures 2a,b and S7), it can be found that Pd 3d_{5/2} is shifted to the higher binding energy, while Cu 2p_{3/2} is shifted to the lower energy. These shifts might be attributed to the complex electronic effects brought about by the formation of Pd–Cu bonds between Pd and Cu. Based on the above XPS analysis, it can be concluded that the Pd and the Cu can adjust the electron structure of each other, in which Pd active sites are electron-rich and thus could facilitate the adsorption of CO₂ and the formation of the key *COOH intermediate.

The local chemical and electronic configurations of Pd and Cu species in the PdCu₃/NC catalyst were further investigated by X-ray absorption near-edge structure (XANES) and extended X-ray absorption fine structure (EXAFS). The K edges of Pd and Cu XANES spectra for the PdCu₃/NC are close to those of Pd foil and Cu foil, respectively (Figure 2c,d), which indicates that the valence state of Pd and Cu in the

PdCu₃/NC is close to 0. This is consistent with the XPS analysis (Figure S6). Furthermore, the Pd–Cu bond was detected by the corresponding Pd (Figure 2e) and Cu (Figure 2f) K-edge Fourier-transformed (FT) EXAFS spectra at about 2.60 (± 0.02) Å.⁴¹ The fitting result of the Pd EXAFS spectrum in Figure 2e shows that the first coordination shell of Pd is affected by Pd–Cu but not by Pd–Pd scattering, indicating that Pd atoms are uniformly distributed on the particles. On the other hand, the first coordination shell of Cu (Figure 2f) is affected by the scattering of Cu–Pd and Cu–Cu but not by the additional scattering of oxygen,⁴¹ which can be confirmed from the EXAFS fitting results (Table S1).

CO₂RR Performances. The CO₂RR catalytic activity of the catalysts was first evaluated in an H-cell with a typical three-electrode system. The linear sweep voltammetry (LSV) curves in Figure 3a show that the current densities of the PdCu₃/NC catalyst in CO₂-saturated KHCO₃ solution are much larger than that in N₂-saturated KHCO₃ solution, indicating that the PdCu₃/NC has high activity for CO₂RR. Moreover, in a CO₂-saturated electrolyte, the PdCu₃/NC catalyst displays a more positive onset reduction potential and a larger current density than that of Pd/NC and Cu/NC, suggesting higher catalytic activity of PdCu₃/NC than that of Pd/NC and Cu/NC. Furthermore, the products after the CO₂RR within the potential range from −0.4 to −0.9 V were investigated. The gas and liquid products were quantified by gas chromatography (GC) and ¹H nuclear magnetic resonance (NMR), respec-

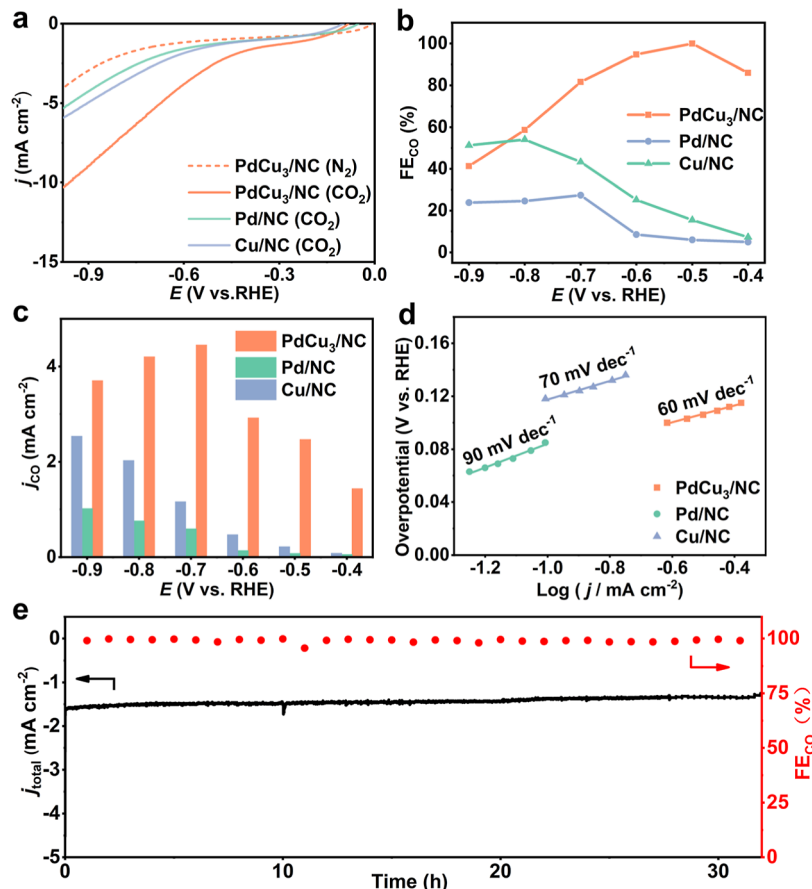


Figure 3. CO_2RR performance measurements. (a) LSV curves of PdCu_3/NC , Pd/NC , and Cu/NC recorded in a CO_2 - or N_2 -saturated 0.1 M KHCO_3 solution. (b) FEs of PdCu_3/NC , Pd/NC , and Cu/NC for CO production at the various potentials. (c) Partial current densities of PdCu_3/NC , Pd/NC , and Cu/NC for CO production. (d) Tafel slopes for PdCu_3/NC , Pd/NC , and Cu/NC catalysts. (e) Stability of total current density and FE_{CO} during 33 h continuous electrolysis on PdCu_3/NC at the applied potential of -0.5 V .

tively. The analysis results reveal that CO is the main product of CO_2RR on PdCu_3/NC . The FE of CO over the PdCu_3/NC catalyst (Figure 3b) is not lower than 40% at the wide applied potentials (-0.4 to -0.9 V) and reaches the optimal value of 99.8% at -0.5 V , superior to highest values of Pd/NC (27.4% at -0.7 V), Cu/NC (54.1% at -0.8 V), and most of other previously reported catalysts (Table S2). Moreover, no liquid reduction product was detected after electrolysis at -0.5 V for 1 h (Figure S8). Furthermore, the partial current density of CO on the PdCu_3/NC catalyst (Figure 3c) increases with more negative applied potential and reaches up to 4.45 mA cm^{-2} at -0.7 V , which is 7.5 and 3.8 times those of Pd/NC (0.59 mA cm^{-2}) and Cu/NC (1.16 mA cm^{-2}), respectively. These results demonstrate the excellent electrocatalytic selectivity of PdCu_3/NC for CO_2RR to CO.

Besides, the Tafel slope for PdCu_3/NC is determined as 60 mV dec^{-1} , which is lower than those of Pd/NC (90 mV dec^{-1}) and Cu/NC (70 mV dec^{-1}). The lower Tafel slope of PdCu_3/NC indicates that the PdCu_3/NC catalyst favors the activation step of ${}^*\text{CO}_2$ to ${}^*\text{COOH}$. The fast activation kinetics of the PdCu_3/NC electrode was further supported by electrochemical impedance spectroscopy (EIS) analysis (Figure S9) that the smaller impedance of the PdCu_3/NC than those of the Pd/NC and Cu/NC suggests a lower charge transfer resistance of the CO_2RR on PdCu_3/NC . Moreover, electrochemical double-layer capacitances (C_{dl}) were measured to explore the cause of the enhanced CO_2RR activity of the PdCu_3/NC catalyst. As

shown in Figure S10, the cyclic voltammograms (CVs) of the catalysts were scanned at the scan rates of 5, 10, 15, 20, and 25 mV s^{-1} . The PdCu_3/NC electrode achieves a C_{dl} value of 69.0 mF cm^{-2} , which is larger than those of Pd/NC (60.4 mF cm^{-2}) and Cu/NC (68 mF cm^{-2}), implying higher surface area and more exposed active sites of the PdCu_3 catalyst, which is beneficial to enhance the CO_2RR activity.

To evaluate the stability of the PdCu_3/NC electrode, electrolysis at the constant applied potential of -0.5 V was carried out. As shown in Figure 3e, a current density of about 1.45 mA cm^{-2} was obtained on the PdCu_3/NC electrode, and the FE for CO production was maintained at about 99.8% throughout the entire process of continuous electrolysis for 33 h. The characterization results of PdCu_3/NC after the electrochemical stability test (Figure S11) show that the PdCu_3 particles keep the crystal structure of the PdCu_3 alloy and have an average size of $217 \pm 1.94 \text{ nm}$, similar to the average size before the stability test ($220 \pm 1.96 \text{ nm}$). Moreover, the exposed (110) facet is not sharp enough, but it still exists. These results demonstrate the high long-term stability of the PdCu_3/NC catalyst for the CO_2RR .

Based on the excellent CO_2RR performances of the PdCu_3/NC catalyst, a Zn– CO_2 battery was assembled (see the schematic diagram in Figure 4a and the digital photograph of the assembled cell in Figure S12). Figure 4b shows the charge–discharge polarization curves of the Zn– CO_2 battery and the open circuit potential of 1.0 V . It exhibits a maximum

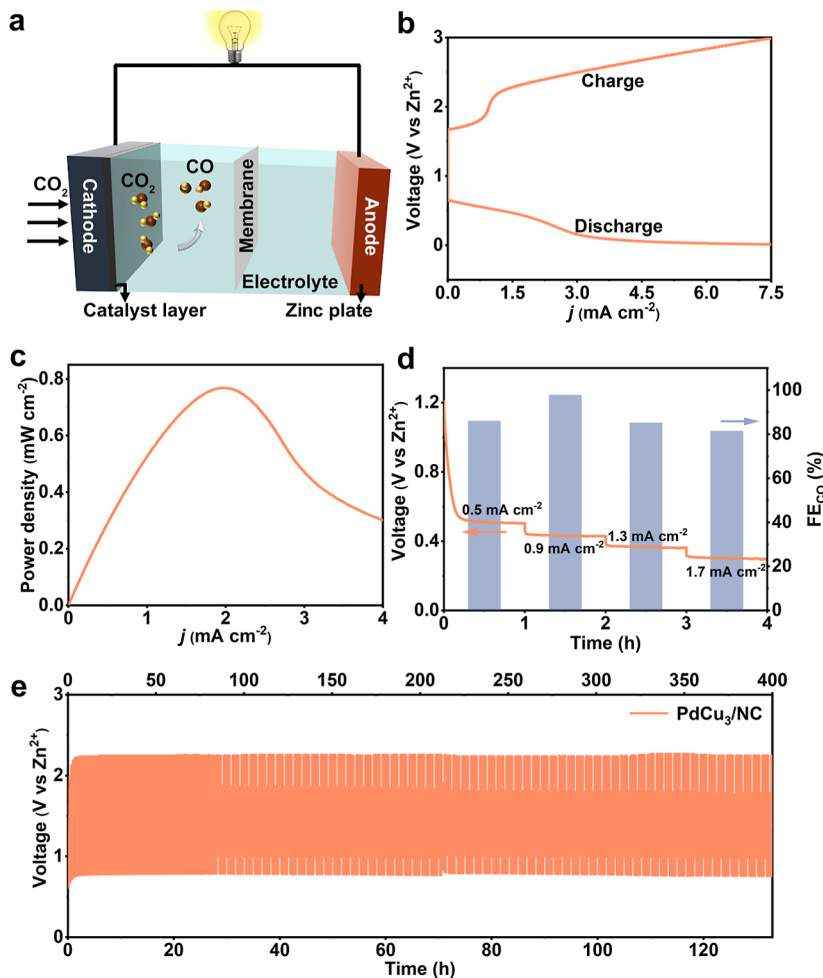


Figure 4. Zn–CO₂ battery based on PdCu₃/NC. (a) Schematic diagram. (b) Charge–discharge voltage curves. (c) Power density curve. (d) Galvanostatic discharge curves at various current densities and the corresponding FEs for CO production. (e) Galvanostatic discharge–charge cycling curves at 0.5 mA cm⁻² for 400 cycles.

power density of 0.77 mW cm⁻² at the current density of 2 mA cm⁻² during the discharge process (Figure 4c). Moreover, at the discharge current density values of 0.5, 0.9, 1.3, and 1.7 mA cm⁻², the Zn–CO₂ battery exhibits the voltage plateaus of 0.58, 0.53, 0.49, and 0.44 V, respectively (Figure 4d), indicating the stable discharge profiles of the battery. Moreover, the corresponding CO production was maintained within the range between 80 and 98%, indicating the excellent conversion ability of CO₂ for CO production and operation durability of the Zn–CO₂ battery device within a wide discharge current range. In addition, a discharge voltage of 0.58 V with the energy efficiency of 99.2% was obtained at a discharge current density of 0.5 mA cm⁻², which is superior to the previously reported Zn–CO₂ batteries (Tables S3 and S4). Moreover, the battery exhibits superior rechargeable durability over the continuous operation for 400 cycles (133 h) at the discharge and charge current density of 0.5 mA cm⁻² (Figure 4e).

DFT Studies. To further elucidate the origin of the high activity of the PdCu₃/NC catalyst for CO₂RR to CO, DFT calculations were performed by using Vienna Ab-initio Simulation Package (VASP). The electrochemical CO₂-to-CO pathway was investigated via a computational hydrogen electrode model. The Pd site (PdCu₃–Pd) and Cu site (PdCu₃–Cu) over the PdCu₃ alloy were selected as the active

sites of the PdCu₃/NC catalysts, respectively. The bare Pd(110) and Cu(110) slabs were used as references. The calculated free energy profiles of the CO₂RR on different active sites are presented in Figure 5. CO₂ activation through *COOH formation is the first proton-coupled electron-transfer step. It is associated with an uphill energy barrier, which requires an overpotential to form reactive intermediates. The computational results show that the required free energy change (ΔG) for the PdCu₃–Pd(110) site from CO₂ to adsorbed *COOH is closest to zero (0.83 eV), lower than that of PdCu₃–Cu(110) (1.38 eV), Pd(110) (0.95 eV), and Cu(110) (1.73 eV). The bond length changes show the same sequence (Table S5). After the formation of adsorbed *COOH, the free-energy pathway is thermodynamically downhill for the second proton-coupled electron-transfer step to form adsorbed *CO. These results illustrate that the first step with *COOH formation is the potential-determining step, and the PdCu₃–Pd active site requires the lowest energy barrier in this step.

The comparison of the Gibbs free energies of CO₂-to-CO pathways over Cu(110), Pd(110), PdCu₃–Pd(110), and PdCu₃–Cu(110) in Figure 5 shows that the PdCu₃–Pd(110) has the lowest Gibbs free energy barrier at the potential-determining step. To unveil the interaction between the Pd and near Cu atoms in PdCu₃, we calculated the Bader charges

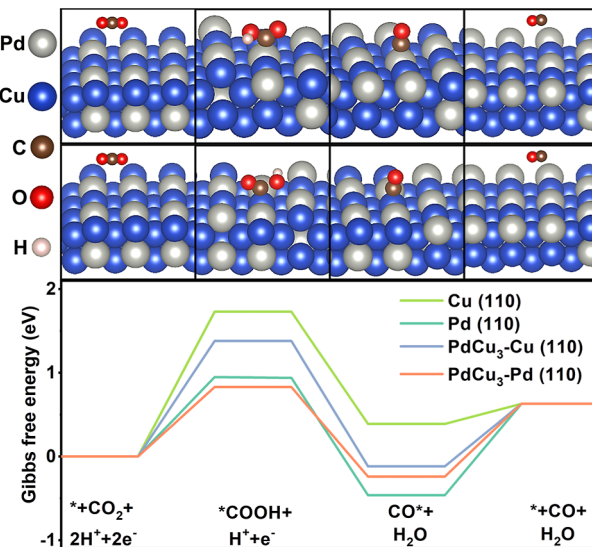


Figure 5. Gibbs free energies of CO₂-to-CO pathways over Cu(110), Pd(110), PdCu₃-Pd(110), and PdCu₃-Cu(110). The inset is the optimized configurations of *CO₂, *COOH, and *CO on PdCu₃-Pd(110) and PdCu₃-Cu(110).

of Cu(110), Pd(110), PdCu₃-Pd(110), and PdCu₃-Cu(110). The Bader charge in Figure S13 shows the Pd atom withdraws 0.25 e from the near Cu atom, leading to stronger adsorption of the Pd atom to the intermediate (*COOH), improving the catalytic activity. Thus, the PdCu₃-Pd(110) active site shows the highest catalytic activity for CO production from CO₂RR.

CONCLUSIONS

In summary, we designed and synthesized a PdCu₃/NC alloy catalyst, confirming that the alloy particles contain a large number of exposed (110) facets. In addition, it is highly efficient in electrochemical CO₂ conversion to CO. The catalyst exhibits superior CO₂ reduction catalytic performances with an FE of 99.8% for CO production at -0.5 V and excellent long-term stability. Moreover, the assembled aqueous Zn-CO₂ battery using the PdCu₃/NC catalyst as cathode material achieves an energy efficiency of up to 99.2% at 0.5 mA cm⁻² and long-term rechargeable stability of up to 133 h. DFT calculations reveal that the (110) plane over the catalyst is the active center for CO₂ activation and rapid formation of the key *COOH intermediate. This work not only designs an electrocatalyst for robust CO₂RR to CO and Zn-CO₂ battery but also provides an in-depth understanding of CO₂RR to CO on alloy electrocatalysts.

EXPERIMENTAL SECTION

Synthesis of PdCu₃/NC. We employed a dissolution and carbonization method to synthesize PdCu₃/NC. Specifically, 1.92 mg of tetraamminedichloropalladium (Cl₂H₁₄N₄OPd), 4.92 mg of cupric chloride (CuCl₂), and 690 mg of hydroxylamine hydrochloride [(NH₃OH)Cl] was dissolved in 40 mL of deionized water by ultrasound. 144 mg of glucose (C₆H₁₂O₆) was dissolved in 40 mL of ethanol. After that, the ethanol solution was mixed with the aqueous solution. And the mixed solution was dried at 80 °C overnight. Afterward, the dried sample was put into a porcelain boat. It was heated from room temperature to 950 °C at a heating rate of 5 °C min⁻¹ under the protection of an Ar atmosphere and maintained for 4 h. After the temperature returned to room temperature, the porcelain was taken out. The resulting product was ground to a fine powder and denoted as PdCu₃/NC. In addition, Pd/NC and Cu/NC were

prepared under the same conditions as PdCu₃/NC, except for 5.78 mg of Cl₂H₁₄N₄OPd but no CuCl₂ added and 11.56 mg of CuCl₂ but no Cl₂H₁₄N₄OPd added, respectively, to keep moles of Pd for Pd/NC and Cu for Cu/NC same as those of the total Pd and Cu for PdCu₃/NC.

Characterizations. X-ray Diffractometry (XRD) measurements were performed with an X-ray diffractometer (Rigaku D/max 2500) in the range of 10 to 90° at a scan speed of 20° min⁻¹. HRTEM images and SAED patterns were achieved using a Thermo Fisher Scientific Talos F200X 200 kV field emission (S)TEM. Atomic-resolution HAADF-STEM images and EDS elemental maps were taken using a Thermo Fisher Scientific Titan Cubed Themis G2 300 probe Cs corrected (S)TEM operating at 200 kV. Nitrogen adsorption/desorption was investigated using an Autosorb-iQ-MP system operated at 77 K, and the specific surface area of the catalyst was finally calculated based on the Brunauer–Emmett–Teller (BET) equation. Concentrations of Pd and Cu elements in samples were determined using inductively coupled plasma-mass spectrometry (ICP-MS). Measurements of the Pd and Cu K-edge X-ray absorption fine structure (XAFS) spectra were performed at the beamline TPS 44A of the National Synchrotron Radiation Research Center (NSRR). XPS spectra were recorded on a Kratos AXIS Ultra DLD system with Al K α radiation as the X-ray source, and the binding energies were calibrated with reference to the C 1s peak at 284.8 eV. The gas products for CO₂ reduction were measured by gas chromatography. The liquid products were tested on an AVANCE III HD 400 MHz Digital NMR spectrometer, and dimethyl sulfoxide was used as an internal standard. All electrochemical tests were carried out on a CHI660D electrochemical workstation.

HAADF-STEM Tomographic Reconstruction. A tilt series of HAADF-STEM images was acquired from -70 to 74° at one interval. During the acquisition, we didn't find any loss of mass or radiation damage on the PdCu₃ particle. A Matlab script package (e-Tomo) written by R. Hovden (Muller group, Cornell) with contributions from H. L. Xin was used to align and reconstruct the acquired tilt series.

Electrode Preparation. 6 mg of the sample powder and 500 μL of 5% Nafion perfluorinated resin solution were dispersed in 500 μL of ethanol by ultrasound for 1 h to form an ink. After that, the catalyst ink was dropped on 1 × 1 cm² of hydrophobic carbon paper as the working electrode with a loading of 0.5 mg cm⁻², and then the carbon paper was dried under a baking lamp for electrochemical test.

Electrochemical Performance Tests. All relevant electrochemical measurements are performed on the CHI660D workstation using "H"-type three-electrode electrochemical cells separated by a Nafion-117 membrane. The platinum foil and Ag/AgCl electrodes were used as counter and reference electrodes, respectively. 0.1 M KHCO₃ (pH = 6.8) aqueous solution is used as the electrolyte for the CO₂ reduction measurement. Before the test, CO₂/N₂ was blown into the system for 30 min at a flow rate of 30 mL min⁻¹ to reach saturation. The CV scan was recorded at a scan rate of 100 mV s⁻¹ in the range of -0.6 to -2.0 V, with at least 50 scans relative to the Ag/AgCl electrode to deactivate the catalyst. After that, LSV curves were recorded at a sweep rate of 10 mV s⁻¹ to evaluate the CO₂ reduction activity of the sample.

The potential of the reversible hydrogen electrode is reasonable

$$E_{\text{RHE}} = E_{\text{Ag}/\text{AgCl}} + 0.059 \text{ pH} + 0.197 \text{ V}$$

To analyze the product distribution of CO₂ reduction reaction. Electrocatalysis was carried out under CO₂ gas bubbling (30 mL min⁻¹) at a given potential for 1 h. The gaseous products were quantified by gas chromatography (Agilent 7890B) equipped with a PoraPLOT Q column and molecular sieve column. The liquid product was analyzed using a ¹H nuclear magnetic resonance (NMR, AVANCE AV III 400 Bruker, Germany) spectrometer.

The electrochemically active surface area (ECSA) is represented by the electrochemical double-layer capacitance (C_{dl}), which is determined by measuring the double-layer charging current at a scan rate of 5, 10, 15, 20, and 25 mV s⁻¹. Electrochemical impedance

spectroscopy (EIS) spectra are recorded in the frequency range of 10 kHz to 10 MHz with an AC amplitude of 5 mV.

Calculation of Faradaic Efficiency. The calculation of FE_{CO} was described as

$$\begin{aligned} \text{FE}_{\text{CO}}(\%) &= (2n \times F)/Q \\ &= (2C_{\text{gas}} \times V_{\text{CO}_2} \times 10^{-3} \times t \times F)/24.8Q \end{aligned}$$

where n is the mol amount of CO generated, F is the Faraday constant (96,485 C mol⁻¹), Q is the total of electric charge, C_{gas} is the volume concentration of the gas-phase products based on the calibration of the GC results, V_{CO_2} is the flow rate of CO₂ (20 mL min⁻¹), and t is electrolysis time (60 min).

Assembly of Zn–CO₂ Battery. PdCu₃/NC is used as the cathode of an aqueous rechargeable Zn–CO₂ electrochemical cell, and a Zn plate with an area of 2 × 5 cm² is used as the anode. 0.8 M KHCO₃ aqueous solution is used as the catholyte, and 0.8 M KOH and 0.02 M Zn(CH₃COO)₂ aqueous solution is used as the anolyte. The cathode chamber and anode chamber are separated by a bipolar membrane. During the discharge process, CO₂ was controlled to flow into the cathode chamber at a rate of 30 mL min⁻¹. All tests were performed in a dual electrolyte system. In addition, the calculation of energy efficiency (EE) was described as

$$\begin{aligned} \text{EE}(\%) &= (n \times F \times V_{\text{discharge}} + \Delta G_{\text{CO}_2 \text{ splitting}} \times \text{FE}_{\text{CO}} \\ &\quad + \Delta G_{\text{H}_2\text{O} \text{ splitting}} \times \text{FE}_{\text{HER}})/(n \times F \times V_{\text{charge}}) \end{aligned}$$

where n is the number of electron transfer in CO₂ reduction reaction, F is the Faraday constant (96,485 C mol⁻¹), $V_{\text{discharge}}$ and V_{charge} are the discharge voltage and charge voltage of the Zn–CO₂ battery, respectively, and $\Delta G_{\text{CO}_2 \text{ splitting}}$ and $\Delta G_{\text{H}_2\text{O} \text{ splitting}}$ are the free energies required for the decomposition of CO₂ and H₂O, respectively.

Density Functional Theory Calculations. All calculations are based on the ab initio DFT calculation method using VASP in the generalized gradient approximation (GGA-PBE). The electronic exchange and correlation energy are described using a plane-wave basic set defined with a 500 eV cut-off energy and the Perdew–Burke–Ernzerhof (PBE) functional. The DFT-D3 method with Becke–Jonson damping is adopted to calculate the van der Waals interactions. PdCu₃(110), Pd(110), and Cu(110) are sampled at 5 × 5 × 1 k points for Brillouin zone integration, where the atomic force and energy convergence standards are 0.02 eV Å⁻¹ and 10⁻⁵ eV, respectively. A vacuum of 20 Å vertically separated the slab from its periodic image. In the geometric optimization process, only the bottom two layers are fixed, while the top two layers are completely relaxed. In free energies calculations, the entropic corrections and zero-point energy (ZPE) have been included.

ASSOCIATED CONTENT

Supporting Information

The Supporting Information is available free of charge at <https://pubs.acs.org/doi/10.1021/acsami.2c09615>.

SEM and TEM images, size distribution, nitrogen adsorption–desorption isotherm, XRD patterns, XPS spectra, NMR spectra, Nyquist plots, ECSA curves and tables of EXAFS fittings analysis and changes in the C–O bond length of CO₂ analysis results, digital photograph of the assembled Zn–CO₂ cell, comparison of CO₂RR activity of Pd- and Cu-based catalysts, comparison of the Zn–CO₂ battery based on the PdCu₃/NC catalyst at different discharge current densities, comparison of Zn–CO₂ battery activity, and Bader charges ([PDF](#))

AUTHOR INFORMATION

Corresponding Authors

Lili Han – State Key Laboratory of Structural Chemistry, Fujian Institute of Research on the Structure of Matter, Chinese Academy of Sciences, Fuzhou 350002, China; Department of Physics and Astronomy, University of California, Irvine, California 92697, United States; Email: llhan@fjirs.ac.cn

Huolin L. Xin – Department of Physics and Astronomy, University of California, Irvine, California 92697, United States; orcid.org/0000-0002-6521-868X; Email: huolin.xin@uci.edu

Authors

Jianwu Dong – State Key Laboratory of Structural Chemistry, Fujian Institute of Research on the Structure of Matter, Chinese Academy of Sciences, Fuzhou 350002, China; Institute for New Energy Materials and Low-Carbon Technologies and Tianjin Key Lab of Photoelectric Materials and Devices, School of Materials Science and Engineering, Tianjin University of Technology, Tianjin 300384, China

Ying Cheng – Institute for New Energy Materials and Low-Carbon Technologies and Tianjin Key Lab of Photoelectric Materials and Devices, School of Materials Science and Engineering, Tianjin University of Technology, Tianjin 300384, China

Ying Li – School of Materials Science and Engineering, Hebei University of Technology, Tianjin 300130, China

Xianyun Peng – Institute for New Energy Materials and Low-Carbon Technologies and Tianjin Key Lab of Photoelectric Materials and Devices, School of Materials Science and Engineering, Tianjin University of Technology, Tianjin 300384, China

Rui Zhang – Department of Physics and Astronomy, University of California, Irvine, California 92697, United States

Hsiao-Tsu Wang – Department of Physics, Tamkang University, New Taipei City 25137, Taiwan; orcid.org/0000-0003-1249-9462

Chunyang Wang – Department of Physics and Astronomy, University of California, Irvine, California 92697, United States

Xiaoyan Li – Department of Electrical and Computer Engineering, University of Toronto, Toronto, Ontario M5S 1A4, Canada

Pengfei Ou – Department of Electrical and Computer Engineering, University of Toronto, Toronto, Ontario M5S 1A4, Canada; orcid.org/0000-0002-3630-0385

Chih-Wen Pao – National Synchrotron Radiation Research Center, Hsinchu 30076, Taiwan

Way-Faung Pong – Department of Physics, Tamkang University, New Taipei City 25137, Taiwan

Zhang Lin – School of Metallurgy and Environment, Central South University, Changsha 410083, China; orcid.org/0000-0002-6600-2055

Jun Luo – Institute for New Energy Materials and Low-Carbon Technologies and Tianjin Key Lab of Photoelectric Materials and Devices, School of Materials Science and Engineering, Tianjin University of Technology, Tianjin 300384, China; orcid.org/0000-0001-5084-2087

Complete contact information is available at: <https://pubs.acs.org/doi/10.1021/acsami.2c09615>

Author Contributions

○J.D., Y.C., and Y.L. contributed equally in this work.

Notes

The authors declare no competing financial interest.

ACKNOWLEDGMENTS

This work was supported by the startup funding of H.L.X. The XAFS/EXAFS spectra obtained from beamline TPS 44A at the National Synchrotron Radiation Research Center (NSRRC) are appreciated.

REFERENCES

- (1) Kuhl, K. P.; Hatsukade, T.; Cave, E. R.; Abram, D. N.; Kibsgaard, J.; Jaramillo, T. F. Electrocatalytic Conversion of Carbon Dioxide to Methane and Methanol on Transition Metal Surfaces. *J. Am. Chem. Soc.* **2014**, *136*, 14107–14113.
- (2) Dinh, C.-T.; Burdyny, T.; Kibria, M. G.; Seifitokaldani, A.; Gabardo, C. M.; García de Arquer, F. P. G. d.; Kiani, A.; Edwards, J. P.; De Luna, P. D.; Bushuyev, O. S.; Zou, C.; Quintero-Bermudez, R.; Pang, Y.; Sinton, D.; Sargent, E. H. CO₂ Electroreduction to Ethylene Via Hydroxide-Mediated Copper Catalysis at An Abrupt Interface. *Science* **2018**, *360*, 783–787.
- (3) Lin, S.; Diercks, C. S.; Zhang, Y.-B.; Kornienko, N.; Nichols, E. M.; Zhao, Y.; Paris, A. R.; Kim, D.; Yang, P.; Yaghi, O. M.; Chang, C. J. Covalent Organic Frameworks Comprising Cobalt Porphyrins for Catalytic CO₂ Reduction in Water. *Science* **2015**, *349*, 1208–1213.
- (4) Wang, G.; Chen, J.; Ding, Y.; Cai, P.; Yi, L.; Li, Y.; Tu, C.; Hou, Y.; Wen, Z.; Dai, L. Electrocatalysis for CO₂ Conversion: from Fundamentals to Value-added Products. *Chem. Soc. Rev.* **2021**, *50*, 4993–5061.
- (5) Nitopi, S.; Bertheussen, E.; Scott, S. B.; Liu, X.; Engstfeld, A. K.; Horch, S.; Seger, B.; Stephens, I. E. L.; Chan, K.; Hahn, C.; Nørskov, J. K.; Jaramillo, T. F.; Chorkendorff, I. Progress and Perspectives of Electrochemical CO₂ Reduction on Copper in Aqueous Electrolyte. *Chem. Rev.* **2019**, *119*, 7610–7672.
- (6) Han, L.; Song, S.; Liu, M.; Yao, S.; Liang, Z.; Cheng, H.; Ren, Z.; Liu, W.; Lin, R.; Qi, G.; Liu, X.; Wu, Q.; Luo, J.; Xin, H. L. Stable and Efficient Single-Atom Zn Catalyst for CO₂ Reduction to CH₄. *J. Am. Chem. Soc.* **2020**, *142*, 12563–12567.
- (7) Zhong, D.; Zhao, Z. J.; Zhao, Q.; Cheng, D.; Liu, B.; Zhang, G.; Deng, W.; Dong, H.; Zhang, L.; Li, J.; Li, J.; Gong, J. Coupling of Cu (100) and (110) Facets Promote Carbon Dioxide Conversion to Hydrocarbons and Alcohols. *Angew. Chem., Int. Ed.* **2021**, *60*, 4879–4885.
- (8) Zhuang, T.-T.; Pang, Y.; Liang, Z.-Q.; Wang, Z.; Li, Y.; Tan, C.-S.; Li, J.; Dinh, C. T.; De Luna, P.; Hsieh, P.-L.; Burdyny, T.; Li, H.-H.; Liu, M.; Wang, Y.; Li, F.; Proppe, A.; Johnston, A.; Nam, D.-H.; Wu, Z.-Y.; Zheng, Y.-R.; Ip, A. H.; Tan, H.; Chen, L.-J.; Yu, S.-H.; Kelley, S. O.; Sinton, D.; Sargent, E. H. Copper Nanocavities Confine Intermediates for Efficient Electrosynthesis of C3 Alcohol Fuels from Carbon Monoxide. *Nat. Catal.* **2018**, *1*, 946–951.
- (9) Hao, X.; An, X.; Patil, A. M.; Wang, P.; Ma, X.; Du, X.; Hao, X.; Abudula, A.; Guan, G. Biomass-derived N-doped Carbon for Efficient Electrocatalytic CO₂ Reduction to CO and Zn-CO₂ Batteries. *ACS Appl. Mater. Interfaces* **2021**, *13*, 3738–3747.
- (10) Khodakov, A. Y.; Chu, W.; Fongarland, P. Advances in The Development of Novel Cobalt Fischer-tropsch Catalysts for Synthesis of Long-chain Hydrocarbons and Clean Fuels. *Chem. Rev.* **2007**, *107*, 1692–1744.
- (11) Mou, S.; Li, Y.; Yue, L.; Liang, J.; Luo, Y.; Liu, Q.; Li, T.; Lu, S.; Asiri, A. M.; Xiong, X.; Ma, D.; Sun, X. Cu₂Sb Decorated Cu Nanowire Arrays for Selective Electrocatalytic CO₂ to CO Conversion. *Nano Res.* **2021**, *14*, 2831–2836.
- (12) Hori, Y.; Wakebe, H.; Tsukamoto, T.; Koga, O. Electrocatalytic Process of CO Selectivity in Electrochemical Reduction of CO₂ at Metal Electrodes in Aqueous Media. *Electrochim. Acta* **1994**, *39*, 1833–1839.
- (13) Birdja, Y. Y.; Pérez-Gallent, E.; Figueiredo, M. C.; Göttle, A. J.; Calle-Vallejo, F.; Koper, M. T. M. Advances and Challenges in Understanding the Electrocatalytic Conversion of Carbon Dioxide to Fuels. *Nat. Energy* **2019**, *4*, 732–745.
- (14) Peterson, A. A.; Nørskov, J. K. Activity Descriptors for CO₂ Electroreduction to Methane on Transition-metal Catalysts. *J. Phys. Chem. Lett.* **2012**, *3*, 251–258.
- (15) Liu, C.; Gong, J.; Gao, Z.; Xiao, L.; Wang, G.; Lu, J.; Zhuang, L. Regulation of The Activity, Selectivity, and Durability of Cu-based Electrocatalysts for CO₂ Reduction. *Sci. China Chem.* **2021**, *64*, 1660–1678.
- (16) Shi, R.; Guo, J.; Zhang, X.; Waterhouse, G. I. N.; Han, Z.; Zhao, Y.; Shang, L.; Zhou, C.; Jiang, L.; Zhang, T. Efficient Wettability-controlled Electroreduction of CO₂ to CO at Au/C Interfaces. *Nat. Commun.* **2020**, *11*, 3028.
- (17) Kim, D.; Xie, C.; Becknell, N.; Yu, Y.; Karamad, M.; Chan, K.; Crumlin, E. J.; Nørskov, J. K.; Yang, P. Electrochemical Activation of CO₂ Through Atomic Ordering Transformations of AuCu Nanoparticles. *J. Am. Chem. Soc.* **2017**, *139*, 8329–8336.
- (18) Dong, W. J.; Yoo, C. J.; Lim, J. W.; Park, J. Y.; Kim, K.; Kim, S.; Lee, D.; Lee, J.-L. Tailoring Electronic Structure of Bifunctional Cu/Ag Layered Electrocatalysts for Selective CO₂ Reduction to CO and CH₄. *Nano Energy* **2020**, *78*, 105168.
- (19) Huang, J.; Mensi, M.; Oveisi, E.; Mantella, V.; Buonsanti, R. Structural Sensitivities in Bimetallic Catalysts for Electrochemical CO₂ Reduction Revealed by Ag-Cu Nanodimers. *J. Am. Chem. Soc.* **2019**, *141*, 2490–2499.
- (20) Ham, Y. S.; Choe, S.; Kim, M. J.; Lim, T.; Kim, S.-K.; Kim, J. J. Electrodeposited Ag Catalysts for The Electrochemical Reduction of CO₂ to CO. *Appl. Catal., B* **2017**, *208*, 35–43.
- (21) Gunji, T.; Ochiai, H.; Ohira, T.; Liu, Y.; Nakajima, Y.; Matsumoto, F. Preparation of Various Pd-based Alloys for Electrocatalytic CO₂ Reduction Reaction-Selectivity Depending on Secondary Elements. *Chem. Mater.* **2020**, *32*, 6855–6863.
- (22) Mun, Y.; Lee, S.; Cho, A.; Kim, S.; Han, J. W.; Lee, J. Cu-Pd Alloy Nanoparticles as Highly Selective Catalysts for Efficient Electrochemical Reduction of CO₂ to CO. *Appl. Catal., B* **2019**, *246*, 82–88.
- (23) Luo, W.; Zhang, J.; Li, M.; Züttel, A. Boosting CO Production in Electrocatalytic CO₂ Reduction on Highly Porous Zn Catalysts. *ACS Catal.* **2019**, *9*, 3783–3791.
- (24) Qin, B.; Li, Y.; Fu, H.; Wang, H.; Chen, S.; Liu, Z.; Peng, F. Electrochemical Reduction of CO₂ into Tunable Syngas Production by Regulating The Crystal Facets of Earth-Abundant Zn Catalyst. *ACS Appl. Mater. Interfaces* **2018**, *10*, 20530–20539.
- (25) Zhu, W.; Kattel, S.; Jiao, F.; Chen, J. G. Shape-controlled CO₂ Electrochemical Reduction on Nanosized Pd Hydride Cubes and Octahedra. *Adv. Energy Mater.* **2019**, *9*, 1802840.
- (26) Wang, W. J.; Hwang, S.; Kim, T.; Ha, S.; Scudiero, L. Corrigendum to 'Study of Carbon Supported CuPd Alloy Nanoparticles with Pd-Rich Surface for the Electrochemical Formate Oxidation and CO₂ Reduction' [Electrochimica Acta, 387 (2021) 138531]. *Electrochim. Acta* **2021**, *389*, 138746.
- (27) Cheng, Y.; Xue, J.; Yang, M.; Li, H.; Guo, P. Bimetallic PdCu Nanoparticles for Electrocatalysis: Multiphase or Homogeneous Alloy? *Inorg. Chem.* **2020**, *59*, 10611–10619.
- (28) Zheng, J.; Zeng, H.; Tan, C.; Zhang, T.; Zhao, B.; Guo, W.; Wang, H.; Sun, Y.; Jiang, L. Coral-like PdCu Alloy Nanoparticles Act as Stable Electrocatalysts for Highly Efficient Formic Acid oxidation. *ACS Sustain. Chem. Eng.* **2019**, *7*, 15354–15360.
- (29) Cai, X.; Wang, A.; Wang, J.; Wang, R.; Zhong, S.; Zhao, Y.; Wu, L.; Chen, J.; Bai, S. Order Engineering on The Lattice of Intermetallic PdCu Co-catalysts for Boosting The Photocatalytic Conversion of CO₂ into CH₄. *J. Mater. Chem. A* **2018**, *6*, 17444–17456.
- (30) Zhang, R.; Yang, M.; Peng, M.; Ling, L.; Wang, B. Understanding The Role of Pd:Cu Ratio, Surface and Electronic Structures in Pd-Cu Alloy Material Applied in Direct Formic Acid Fuel Cells. *Appl. Surf. Sci.* **2019**, *465*, 730–739.

- (31) Zhu, W.; Zhang, L.; Yang, P.; Chang, X.; Dong, H.; Li, A.; Hu, C.; Huang, Z.; Zhao, Z. J.; Gong, J. Morphological and Compositional Design of Pd-Cu Bimetallic Nanocatalysts with Controllable Product Selectivity toward CO₂ Electroreduction. *Small* **2018**, *14*, 1703314.
- (32) Han, L.; Ren, Z.; Ou, P.; Cheng, H.; Rui, N.; Lin, L.; Liu, X.; Zhuo, L.; Song, J.; Sun, J.; Luo, J.; Xin, H. L. Modulating Single-atom Palladium Sites with Copper for Enhanced Ambient Ammonia Electrosynthesis. *Angew. Chem., Int. Ed.* **2021**, *60*, 345–350.
- (33) Han, L.; Hou, M.; Ou, P.; Cheng, H.; Ren, Z.; Liang, Z.; Boscoboinik, J. A.; Hunt, A.; Waluyo, I.; Zhang, S.; Zhuo, L.; Song, J.; Liu, X.; Luo, J.; Xin, H. L. Local Modulation of Single-Atomic Mn Sites for Enhanced Ambient Ammonia Electrosynthesis. *ACS Catal.* **2020**, *11*, 509–516.
- (34) Jiang, X.; Koizumi, N.; Guo, X.; Song, C. Bimetallic Pd-Cu Catalysts for Selective CO₂ Hydrogenation to Methanol. *Appl. Catal., B* **2015**, *170–171*, 173–185.
- (35) Jana, R.; Datta, A.; Malik, S. Tuning Intermediate Adsorption in Structurally Ordered Substituted PdCu₃ Intermetallic Nanoparticles for Enhanced Ethanol Oxidation Reaction. *Chem. Commun.* **2021**, *57*, 4508–4511.
- (36) Sheng, J.; Kang, J.; Ye, H.; Xie, J.; Zhao, B.; Fu, X.-Z.; Yu, Y.; Sun, R.; Wong, C.-P. Porous Octahedral PdCu Nanocages as Highly Efficient Electrocatalysts for The Methanol Oxidation Reaction. *J. Mater. Chem. A* **2018**, *6*, 3906–3912.
- (37) Venezia, A. M.; Liotta, L. F.; Deganello, G.; Schay, Z.; Guczi, L. Characterization of Pumice-supported Ag-Pd and Cu-Pd Bimetallic Catalysts by X-ray Photoelectron Spectroscopy and X-ray Diffraction. *J. Catal.* **1999**, *182*, 449–455.
- (38) Sarfraz, S.; Garcia-Esparza, A. T.; Jedidi, A.; Cavallo, L.; Takanabe, K. Cu-Sn Bimetallic Catalyst for Selective Aqueous Electroreduction of CO₂ to CO. *ACS Catal.* **2016**, *6*, 2842–2851.
- (39) Han, Y.; Wang, Z.; Han, X.; Fang, W.; Zhou, Y.; Lei, K.; You, B.; Park, H. S.; Xia, B. Y. Selectively Converting Carbon Dioxide to Syngas over Intermetallic AuCu Catalysts. *ACS Sustain. Chem. Eng.* **2021**, *9*, 2609–2615.
- (40) Liang, Z. Q.; Zhuang, T. T.; Seifitokaldani, A.; Li, J.; Huang, C. W.; Tan, C. S.; Li, Y.; De Luna, P.; Dinh, C. T.; Hu, Y.; Xiao, Q.; Hsieh, P. L.; Wang, Y.; Li, F.; Quintero-Bermudez, R.; Zhou, Y.; Chen, P.; Pang, Y.; Lo, S. C.; Chen, L. J.; Tan, H.; Xu, Z.; Zhao, S.; Sinton, D.; Sargent, E. H. Copper-on-nitride Enhances The Stable Electrosynthesis of Multi-carbon Products from CO₂. *Nat. Commun.* **2018**, *9*, 3828.
- (41) Yin, Z.; Gao, D.; Yao, S.; Zhao, B.; Cai, F.; Lin, L.; Tang, P.; Zhai, P.; Wang, G.; Ma, D.; Bao, X. Highly Selective Palladium-copper Bimetallic Electrocatalysts for The Electrochemical Reduction of CO₂ to CO. *Nano Energy* **2016**, *27*, 35–43.

□ Recommended by ACS

Hydrogen Spillover-Accelerated Selective Hydrogenation on WO₃ with ppm-Level Pd

Yu Sun, Sai Zhang, et al.

APRIL 11, 2023

ACS APPLIED MATERIALS & INTERFACES

READ ↗

Tuning the Interaction between Pd and MgAl₂O₄ To Enhance the Dehydrogenation Activity and Selectivity of Dodecahydro-N-ethylcarbazole

Bin Wang, Tao Fang, et al.

MARCH 29, 2023

ACS SUSTAINABLE CHEMISTRY & ENGINEERING

READ ↗

Designing a Robust Palladium Catalyst for Formic Acid Dehydrogenation

Zupeng Chen, Matthias Beller, et al.

MARCH 27, 2023

ACS CATALYSIS

READ ↗

Promoting Effect of Nitride as Support for Pd Hydridechlorination Catalyst

Xiaotian Hua, Rui Liu, et al.

MARCH 20, 2023

LANGMUIR

READ ↗

Get More Suggestions >